

Weyl semimetal in ultra-thin film of topological insulator multilayer

S. A. Owerre^{1,2,*}

¹*African Institute for Mathematical Sciences, 6 Melrose Road, Muizenberg, Cape Town 7945, South Africa.*

²*Perimeter Institute for Theoretical Physics, 31 Caroline St. N., Waterloo, Ontario N2L 2Y5, Canada.*

In ultra-thin film of topological insulator, the hybridization between the top and bottom surfaces opens an energy gap and forms two degenerate quantum anomalous Hall states, which give rise to a quantum spin Hall state. In this paper, we demonstrate that a Weyl semimetal can be realized in an ultra-thin film of topological insulator heterostructure in a similar way to that of the surface state of a strong three-dimensional (3D) topological insulator studied by Burkov and Balents. We find that the system realizes both 3D quantum anomalous Hall phase and 3D quantum spin Hall phase, and the Weyl nodes occur at zero energy when both time-reversal symmetry and inversion symmetry are explicitly broken by the magnetic field and the structure inversion asymmetry of the thin film.

I. INTRODUCTION

Weyl semimetal is a name given to specific materials that host Weyl fermions in three dimensions in which time-reversal symmetry (\mathcal{T}) or inversion symmetry (\mathcal{I}) is explicitly broken¹⁻³. The low-energy Hamiltonian near the isolated band touching points (Weyl points) is reminiscent of the Weyl equation or massless Dirac equation from high energy physics^{4,5}, given by $H = \pm v_F \boldsymbol{\sigma} \cdot \mathbf{k}$, where $\boldsymbol{\sigma}$ is the triplet Pauli matrices and \mathbf{k} is a 3-component Brillouin zone momentum and \pm denote the chirality. In contrast to two-dimensional (2D) electron systems^{7,9}, the Weyl point is robust to any external perturbations as the three components of the momentum are required to vanish at the point of degeneracy. The breaking of \mathcal{T} or \mathcal{I} separates the Weyl nodes in momentum space and they become topologically stable¹¹. The topological properties of Weyl points are manifested as monopoles of Berry flux in the Brillouin zone (BZ) with point-like Fermi arcs surface states⁵.

However, when the Fermi arcs are not point-like but tilted, there is another possibility of Weyl semimetals dubbed type-II Weyl semimetals¹². In recent years, there have been many proposals of systems that host Weyl semimetal phases. The pyrochlore iridates^{5,13} are well-known as one of the materials in which a Weyl semimetal phase can be observed. A very simple model using the surface states of a strong 3D TI heterostructure has been proposed^{1,2,14,15}. Weyl semimetal phase has been proposed in the magnetically doped topological band insulators¹⁶. There is also a toy tight binding model proposal that captures the existence of Weyl semimetal phase¹⁷⁻¹⁹. Recently, Weyl semimetal has been discovered experimentally in photonic crystals²¹. The experimental realization of Weyl semimetal in TaAs has also been reported using angle-resolved photoemission spectroscopy²²⁻²⁴.

In this letter, we demonstrate that Weyl semimetal can be realized in an alternating ordinary insulator and thin film of topological insulator (TI) multilayer. This heterostructure has some similarities to the model studied by Burkov and Balents¹. However, the ultrathin film of

TI possesses a different Hamiltonian²⁵⁻²⁸. Besides, they can be easily grown in the laboratory and have been realized in most experiments in ultrathin Bi₂Se₃ and Bi₂Te₃ films²⁹⁻³¹. In experiments, it is indeed possible to grow quintuple layers (QL) of an ultrathin film of TI, in which two Bi and three Se or Te layers are stacked together.

In particular, we show that in the absence of a magnetic field and structure inversion asymmetry the thin film of TI multilayer captures a phase with two Dirac nodes, which annihilate each other at the phase transition point and opens a gap to a 3D QSH phase. In the presence of an external magnetic field, however, the system breaks \mathcal{T} but preserves \mathcal{I} . We find that the magnetic field introduces a 3D QAH phase. We also find a phase with two Weyl points separated in momentum space (Weyl semimetal) and an ordinary insulator. Adding a structure inversion asymmetry term introduces a potential difference between the top and bottom surfaces of each layer and breaks \mathcal{I} but preserves \mathcal{T} , while the magnetic field breaks \mathcal{T} but preserves \mathcal{I} , and the whole system then breaks both symmetries. In this case, the system still produces a Weyl semimetal phase and the nodes still occur at zero energy. We also analyze the effects of an orbital magnetic field and obtain the Landau level spectra of the system. The zero Landau levels capture the appearance of Weyl semimetal phase in the vicinity of the bulk gap. Finally, we show that in the absence of the magnetic field and the structure inversion asymmetry, the continuum limit of the ultrathin film TI multilayer is the same as the continuum limit of the toy tight binding Hamiltonian of Weyl semimetal¹⁷⁻²⁰.

II. MODEL

Following Burkov and Balents¹, we study a simple Hamiltonian of an ultrathin film of topological insulator heterostructure (Fig. 1). The Hamiltonian is governed by

$$H = \sum_{\mathbf{k}_\perp, ij} a_{\mathbf{k}_\perp i}^\dagger \mathcal{H}_{ij} a_{\mathbf{k}_\perp j}, \quad (1)$$

where

$$\begin{aligned} \mathcal{H}_{ij} = & v_F(\hat{z} \times \boldsymbol{\sigma}) \cdot \mathbf{k}_\perp \delta_{ij} + \left(\frac{t_S}{2} - t_\perp k_\perp^2\right) \tau_z \sigma_z \delta_{ij} \\ & + b \tau_x \delta_{ij} + \gamma \sigma_z \delta_{ij} + \frac{t_D}{2} \frac{(\delta_{j,i+1} + \delta_{j,i-1})}{2} \tau_z \sigma_z. \end{aligned} \quad (2)$$

Here, $\boldsymbol{\sigma}$ are the Pauli matrices on the real spin space and $\boldsymbol{\tau}$ are the *which surface* pseudo spins. $\mathbf{k}_\perp = (k_x, k_y)$ is a 2D momentum vector in the BZ. The indices i, j label distinct thin film layers and v_F is the Fermi velocity.

The first two terms in Eq. (2) describe the low-energy Hamiltonian of a single 2D ultrathin film of TI layer^{25–28}. The parameters t_S and t_\perp are the hybridization potentials that couple the top and bottom surfaces of the same thin film layer for small k_\perp and large k_\perp respectively. The parameter b denotes the structure inversion asymmetry term which will be inevitably present when growing the system in Fig. (1). In fact, the first three terms in Eq. (2) have recently been studied³². The electrostatic potential introduces a potential difference of $2b$ between the top and bottom surfaces. The Zeeman splitting is $\gamma = g\mu_B B$ and can be induced by depositing a ferromagnetic material on the thin film (magnetic doping) or directly applying a magnetic field. Here g is the Landé g -factor of the thin film, μ_B is the Bohr magneton, and B is the magnetic field. The new parameter we introduce in Eq. (2) is t_D . This is the hybridization potential that couples the top and bottom surfaces of neighbouring thin film layers along the growth z -direction.

The parameters b , t_\perp , t_S , and t_D depend on the thickness of the thin film. The first three parameters have been determined both numerically^{26–28} and experimentally^{29,30}. The new parameter t_D can also be determined by growing the multilayer in Fig. (1). Without loss of generality we assume all the parameters to be positive $b, t_\perp, t_S, t_D > 0$, which is indeed the case in most experiments in 2D thin films ($t_D = 0$)^{29,30}.

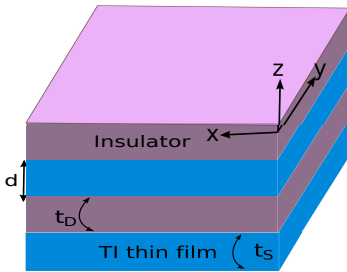


FIG. 1: Color online. Schematic sketch of four array of alternating ordinary insulator and thin film topological insulators (TI), where t_S is the hybridization potential that couples the top and bottom surfaces in the same thin film layer, t_D is the hybridization potential on neighbouring thin film layers, d is the spacing between film layers.

III. ZERO FIELD AND ZERO POTENTIAL

Let us first consider a very simple case $\gamma = b = 0$ in Eq. (2). To study the topological properties of this system it is expedient to Fourier transform into momentum space along the growth z -direction. We obtain $H = \sum_{\mathbf{k}} a_{\mathbf{k}}^\dagger \mathcal{H}(\mathbf{k}) a_{\mathbf{k}}$, with

$$\mathcal{H}(\mathbf{k}) = v_F(\hat{z} \times \boldsymbol{\sigma}) \cdot \mathbf{k}_\perp + \hat{\Delta}(k_z, k_\perp) \sigma_z, \quad (3)$$

where

$$\hat{\Delta}(k_z, k_\perp) = \left(\frac{t_S}{2} - t_\perp k_\perp^2 + \frac{t_D}{2} \cos(k_z d) \right) \tau_z. \quad (4)$$

One distinguishing feature of $\hat{\Delta}$ is that it contains quadratic terms in the continuum limit, which is in fact a common feature of toy tight binding models of Weyl semimetal^{17,20}. For the model in Eq. (3), the system preserves \mathcal{T} and \mathcal{I} . It may be written as a four-component Dirac fermions

$$\mathcal{H}(\mathbf{k}) = \begin{pmatrix} \mathcal{H}_\uparrow(\mathbf{k}) & 0 \\ 0 & \mathcal{H}_\downarrow^*(-\mathbf{k}) \end{pmatrix}, \quad (5)$$

where the arrow denote the top surface and the bottom surface is related by $\mathcal{H}_\downarrow^*(-\mathbf{k}) = \sigma_y \mathcal{H}_\uparrow(\mathbf{k}) \sigma_y$ under a unitary transformation using $U = \text{diag}(\sigma_0, i\sigma_y)$, where σ_0 is a 2×2 identity matrix. Under time-reversal symmetry and inversion symmetry, we have

$$\mathcal{T} : \mathcal{H}(\mathbf{k}) \rightarrow \mathcal{T} \mathcal{H}^*(-\mathbf{k}) \mathcal{T}^{-1}, \quad (6)$$

$$\mathcal{I} : \mathcal{H}(\mathbf{k}) \rightarrow \mathcal{I} \mathcal{H}(-\mathbf{k}) \mathcal{I}^{-1}. \quad (7)$$

The \mathcal{T} operator is $\mathcal{T} = \tau_0 \otimes \Theta$, where $\Theta = i\sigma_y \mathcal{K}$ and \mathcal{K} is the complex conjugation. The inversion operator for this system is $\mathcal{I} = \tau_z \otimes \sigma_z$. Note that $\mathcal{T}^2 = -1$ and $\mathcal{I}^2 = 1$. The system thus describes a 3D Dirac semimetal. The eigenvalues of $\hat{\Delta}(k_z, k_\perp)$ are $\pm \Delta(k_z, k_\perp)$, where

$$\Delta(k_z, k_\perp) = \frac{t_S}{2} - t_\perp k_\perp^2 + \frac{t_D}{2} \cos(k_z d). \quad (8)$$

The corresponding eigenspinors are

$$u^\uparrow = \begin{pmatrix} 1 \\ 0 \end{pmatrix}; \quad u^\downarrow = \begin{pmatrix} 0 \\ 1 \end{pmatrix}. \quad (9)$$

The Hamiltonian then becomes

$$\mathcal{H}_s(\mathbf{k}) = v_F(\hat{z} \times \boldsymbol{\sigma}) \cdot \mathbf{k}_\perp + s \Delta(k_z, k_\perp) \sigma_z, \quad (10)$$

where $s = \pm (\uparrow, \downarrow)$.

Similar to Burkov and Balents¹ model at zero magnetic field, $\Delta(k_z, k_\perp)$ vanishes at $t_S/t_D = 1$ for $k_z = \pi/d$ and at $t_S/t_D = -1$ for $k_z = 0$, only if $k_x = k_y = 0$. The Hamiltonian is easily diagonalized. The energy eigenvalues are two-fold degenerate as expected from Kramers

theorem due to time-reversal symmetry. They are given by

$$\epsilon_\eta(\mathbf{k}) = \eta \sqrt{v_F^2 k_\perp^2 + \Delta^2} = \eta \epsilon_{\mathbf{k}}, \quad (11)$$

where $\Delta = \Delta(k_z, k_\perp)$ and $\eta = \pm$ labels the conduction and the valence bands respectively, and the eigenvectors are

$$\chi_\eta(\Delta) = \frac{1}{\sqrt{2}} \begin{pmatrix} \sqrt{1 - \eta \frac{\Delta}{\epsilon_{\mathbf{k}}}}, -i\eta e^{-i\theta_{\mathbf{k}_\perp}} \sqrt{1 + \eta \frac{\Delta}{\epsilon_{\mathbf{k}}}} \end{pmatrix}^T, \quad (12)$$

where $\theta_{\mathbf{k}_\perp} = \tan^{-1}(k_y/k_x)$. Hence, the eigenspinors of the complete system are the tensor product of Eqs. (9) and (12) given by

$$\psi_\eta^\uparrow = \begin{pmatrix} \chi_\eta(\Delta) \\ \mathbf{0} \end{pmatrix} \quad \text{and} \quad \psi_\eta^\downarrow = \begin{pmatrix} \mathbf{0} \\ \chi_\eta(-\Delta) \end{pmatrix}. \quad (13)$$

For $t_D \neq 0$, the system can be regarded as two copies of 3D two-band QAH insulators, each breaks \mathcal{T} and the whole system is \mathcal{T} -invariant. There are two Dirac nodes located along the line $k_x = k_y = 0$, $k_z = \pi/d \pm k_z^0$, where

$$k_z^0 = \frac{1}{d} \arccos\left(\frac{t_S}{t_D}\right). \quad (14)$$

We see that the \mathcal{T} -invariant ultrathin film TI multi-

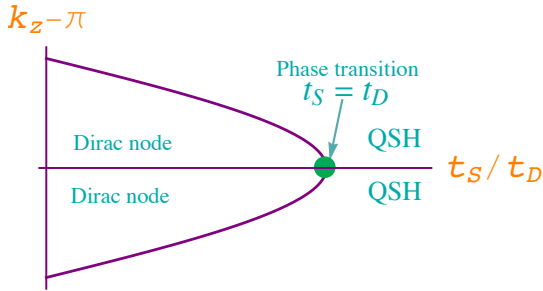


FIG. 2: Color online. The topological phase transition in $(t_S/t_D, k_z)$ space at $\gamma = b = 0$. The two Dirac nodes are not protected by symmetry and they are required to annihilate at the phase transition point $t_S = t_D$ giving rise to fully gapped phase (QSH phase) for $t_S > t_D$.

layer captures a phase with two Dirac nodes along the k_z -axis for $t_S < t_D$. However, since having only \mathcal{T} and \mathcal{I} symmetries cannot produce stable Dirac points with non-trivial topological invariant number^{4,33}, additional symmetry (e.g. crystal rotational symmetry) is required to stabilize the Dirac points as in the case of 3D Dirac semimetal proposed in Cd_3As_2 and Na_3Bi ^{34–36}. Thus, in the present model the Dirac points must annihilate each other (see Fig. 2). This is what happens at the topological phase transition point $t_S/t_D = 1$. A gap reopens for $t_S > t_D$, which corresponds to a 3D QSH phase. The topological invariant number, ν , in the vicinity of the Dirac points must vanish by time-reversal symmetry^{4,33}.

In the 3D QSH phase ($t_S > t_D$), we compute the Z_2 topological number by diagonalizing the parity operator in the occupied bands at the phase transition point $k_x = k_y = 0$, $k_z = \pi/d$, using the method of Fu and Kane³⁷. We obtain

$$(-1)^\nu = -\text{sgn}(t_S - t_D). \quad (15)$$

IV. NONZERO FIELD AND ZERO POTENTIAL

When a nonzero magnetic field is applied to the system, the 3D Dirac semimetal can be driven into various topologically distinct phases since time-reversal symmetry is broken^{1,34}. Keeping $b = 0$ preserves inversion symmetry. In this case, the resulting Hamiltonian is given by

$$\mathcal{H}_s(\mathbf{k}) = v_F(\hat{z} \times \boldsymbol{\sigma}) \cdot \mathbf{k}_\perp + m_s(k_z, k_\perp)\sigma_z, \quad (16)$$

where $m_s(k_z, k_\perp) = \gamma + s\Delta(k_z, k_\perp)$. The above Hamiltonian (Eq. 16) is very similar to that of Burkov and Balents¹ except for the $\Delta(k_z, k_\perp)$ function. The effect of breaking time-reversal symmetry is that the degeneracy of each Dirac node split into two Weyl nodes (the kissing of two non-degenerate bands) separated in momentum space. This is clearly seen by diagonalizing the Hamiltonian with $\gamma \neq 0$. The eigenvalues are given by

$$\epsilon_{\eta s}(\mathbf{k}) = \eta \epsilon_s(\mathbf{k}) = \eta \sqrt{v_F^2 k_\perp^2 + m_s^2(k_z, k_\perp)}. \quad (17)$$

The eigenspinors are given by Eq. (13) with the replacement $\epsilon(\mathbf{k}) \rightarrow \epsilon_\pm(\mathbf{k})$; $\pm\Delta(k_z, k_\perp) \rightarrow m_\pm(k_z, k_\perp)$. Now the Dirac nodes are given by the solutions of $m_-(k_z, k_\perp) = 0$. Note that the positive mass never changes sign. The Dirac nodes are located at $k_x = k_y = 0$, $k_z = \pi/d \pm k_z^0$, where

$$k_z^0 = \frac{1}{d} \arccos\left(1 - \frac{2}{t_D}[\gamma - \frac{t_S - t_D}{2}]\right). \quad (18)$$

We denote the phase boundaries by $\gamma_\pm = (t_S \pm t_D)/2$, where $\gamma_+ > |\gamma_-|$. The phase diagram comprises an ordinary insulator phase for $\gamma < |\gamma_-|$ and a 3D Weyl semimetal phase in the regime $|\gamma_-| < \gamma < \gamma_+$, with two Dirac nodes. For $\gamma > \gamma_+$ the system transits into a 3D QAH phase. The Chern number depends only on the $\tau_z = -1$ sector. It can be computed using the eigenstates of the occupied bands in the $\tau_z = -1$ sector, we obtain³⁸

$$\mathcal{C}^-(k_z) = -\frac{1}{2}[\text{sgn}(\gamma - \Delta(k_z, 0)) + \text{sgn}(t_\perp)]. \quad (19)$$

The total conductivity is quantized at $k_z^0 = \pi/d$ or $k_z = 0$. It is given by

$$\sigma_{xy} = -\frac{e}{2\hbar d}[\text{sign}(\gamma - \gamma_+) + \text{sign}(t_\perp)]. \quad (20)$$

V. NONZERO FIELD AND NONZERO POTENTIAL

Now we study the effects of breaking both time-reversal symmetry and inversion symmetry. This can be achieved by turning on the structure inversion asymmetry, $b \neq 0$. The Hamiltonian is given by

$$\mathcal{H}(\mathbf{k}) = v_F(\hat{z} \times \boldsymbol{\sigma}) \cdot \mathbf{k}_\perp + [\gamma + \hat{\Delta}(k_z, k_\perp)]\sigma_z + b\tau_x. \quad (21)$$

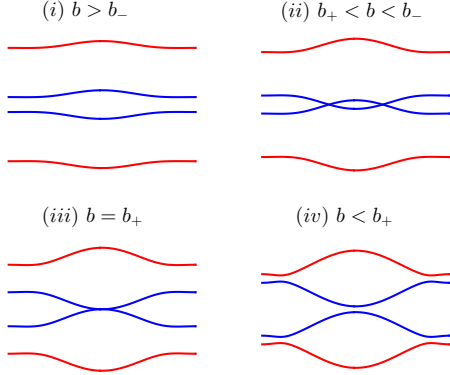


FIG. 3: Color online. The energy dispersion of Eq. (3) along the growth direction, that is k_z direction in momentum space with $k_x = k_y = 0$. We take $t_S < t_D$, $b < \gamma$, and $\gamma > \gamma_\pm$.

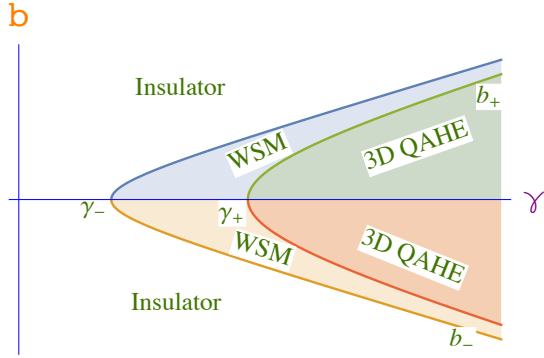


FIG. 4: Color online. The phase diagram of the thin film heterostructure with the same parameter regimes in Fig. (3). There are three regimes comprising a Weyl semimetal (WSM), a 3D QAHE effect, and an ordinary insulator bounded by the phase boundaries in Eq. (26).

The structure inversion asymmetry breaks inversion symmetry but preserves time-reversal symmetry (if we take $\mathcal{T} = \tau_x \otimes \Theta$), whereas the magnetic field breaks time-reversal symmetry and preserves inversion symmetry. The whole system thus breaks both symmetries and a Weyl semimetal phase is also possible¹⁵. The eigenvalues of Eq. (21) are given by

$$\epsilon_{\eta s}(\mathbf{k}) = \eta \sqrt{[\Delta(k_z, k_\perp) \cos \theta(k_\perp)]^2 + m_s^2(k_z, k_\perp)}; \quad (22)$$

where $m_s(k_z, k_\perp) = \xi + s\chi$,

$$\xi = \sqrt{v_F^2 k_\perp^2 + \gamma^2}; \quad \chi = \sqrt{b^2 + \Delta^2 \sin^2 \theta(k_\perp)}; \quad (23)$$

$$\sin \theta(k_\perp) = \frac{\gamma}{\xi}; \quad \cos \theta(k_\perp) = \frac{v_F k_\perp}{\xi}. \quad (24)$$

The Weyl nodes are given by the solution of $m_- = 0$. We obtain $k_z = \pi/d \pm k_z^0$, where

$$k_z^0 = \frac{1}{d} \arccos \left(1 - \frac{2}{t_D} [\sqrt{\gamma^2 - b^2} - \frac{t_S - t_D}{2}] \right), \quad (25)$$

and $b < \gamma$. For $b \gg \gamma$, there is neither a circular node nor a Weyl node as can be verified from Eq. (22). The phase boundaries are given by

$$b_\pm = \eta \sqrt{\gamma^2 - \gamma_\pm^2}, \quad (26)$$

where $b_+ < b_-$. The Chern number in Eq. (19) only changes by the phase boundary Eq. (26).

Figures (3) and (4) show the energy bands and the phase diagram respectively. Approaching the phase boundaries from the upper bound, we see that the system is an ordinary insulator for $b > b_-$. The two Weyl nodes are located at the intermediate regime $b_+ < b < b_-$. The Weyl nodes, however, occur at the zero energy despite broken time-reversal and inversion symmetries. At $b = b_+$ they are annihilated at the center of the BZ $k_z^0 = \pi/d$ or $k_z = 0$. For $b < b_+$ the system is again fully gapped, which corresponds to a 3D QAHE phase.

VI. ORBITAL MAGNETIC FIELD EFFECTS

Next, we study the effects of an orbital magnetic field through the Peierls substitution, $\mathbf{k}_\perp \rightarrow -i\nabla + \frac{e}{c}\mathbf{A}$. In the Landau gauge the vector potential, $\mathbf{A} = -yB\hat{x}$ and corresponds to a magnetic field along the growth z -direction. Introducing the operator $\boldsymbol{\pi} = -i\nabla + \frac{e}{c}\mathbf{A}$, Eq. (3) can be written as

$$\mathcal{H}(k_z) = v_F(\pi_y \sigma_x - \pi_x \sigma_y) + [\gamma + \hat{\Delta}(k_z, \pi_\perp)]\sigma_z + b\tau_x, \quad (27)$$

where

$$\hat{\Delta}(k_z, \pi_\perp) = \left[\frac{t_S}{2} + \frac{t_D}{2} \cos(k_z d) - t_\perp (\pi_x^2 + \pi_y^2) \right] \tau_z. \quad (28)$$

The Landau level spectrum is obtained by introducing the creation and annihilation operators:

$$\pi_x = \frac{a^\dagger + a}{l_B \sqrt{2}}; \quad \pi_y = -i \frac{a^\dagger - a}{l_B \sqrt{2}}, \quad (29)$$

where $l_B^2 = c/eB$ is the magnetic length. In terms of a and a^\dagger the Hamiltonian becomes

$$\mathcal{H}(k_z) = i\omega_B \sqrt{2} (\sigma^+ a - \sigma^- a^\dagger) + [\gamma + \Delta \tau_z] \sigma_z + b\tau_x, \quad (30)$$

where

$$\Delta(k_z; a^\dagger, a) = \left[\frac{t_S}{2} + \frac{t_D}{2} \cos(k_z d) - \omega_0 \left(a^\dagger a + \frac{1}{2} \right) \right]. \quad (31)$$

Here, $\omega_B = v_F/l_B$ is the magnetic frequency and $\omega_0 = 2t_\perp/l_B^2$ is the harmonic oscillator frequency. The eigenvalue equation may be written as

$$\begin{pmatrix} h_L(k_z) & b \\ b & h_R(k_z) \end{pmatrix} \begin{pmatrix} \psi_L \\ \psi_R \end{pmatrix} = \epsilon(k_z) \begin{pmatrix} \psi_L \\ \psi_R \end{pmatrix}, \quad (32)$$

where

$$h_{L/R}(k_z) = i\omega_B \sqrt{2}(\sigma^+ a - \sigma^- a^\dagger) + [\gamma \pm \Delta(k_z; a^\dagger, a)]\sigma_z, \quad (33)$$

and $\psi_{L/R}$ are two-component spinors.

Equation (32) shows that the potential b acts as a mass term in 4×4 Dirac equation. When this mass, b , vanishes, ψ_L and ψ_R decouples into two separate Weyl equations. For the two coupled Weyl fermions $b \neq 0$, the eigenvectors are spinors given by

$$\psi_{L/R;n \neq 0} = \begin{pmatrix} \alpha_{L/R} u_{n-1} \\ \beta_{L/R} u_n \end{pmatrix}, \quad (34)$$

where $\alpha_{L/R}, \beta_{L/R}$ are constants to be determined. The operators satisfy $au_n = \sqrt{n}u_{n-1}$; $a^\dagger u_n = \sqrt{n+1}u_{n+1}$. Hence, Eq. (32) yields a secular equation for $\alpha_{L/R}$ and $\beta_{L/R}$

$$\begin{vmatrix} \mathcal{R}_1 - \epsilon_n & i\omega_B \sqrt{2n} & b & 0 \\ -i\omega_B \sqrt{2n} & \mathcal{R}_2 - \epsilon_n & 0 & b \\ b & 0 & \mathcal{R}_3 - \epsilon_n & i\omega_B \sqrt{2n} \\ 0 & b & -i\omega_B \sqrt{2n} & \mathcal{R}_4 - \epsilon_n \end{vmatrix} = 0, \quad (35)$$

where

$$\mathcal{R}_{1,2} = \frac{\omega_0}{2} \pm \mathcal{R}_n^+(k_z); \quad \mathcal{R}_{3,4} = -\frac{\omega_0}{2} \pm \mathcal{R}_n^-(k_z), \quad (36)$$

$$\mathcal{R}_n^s(k_z) = \gamma + s \left[\frac{t_S}{2} + \frac{t_D}{2} \cos(k_z d) - \omega_0 n \right]. \quad (37)$$

The solutions for $\epsilon_n(k_z)$ correspond to the Landau level spectrum. Next, we drop the zero point energy of the harmonic oscillator in Eq. (36), that is $\omega_0/2$, which can be eliminated by normalizing the oscillator energy. Thus, Eq. (35) is amenable to analytical solution and the Landau level are given by

$$\epsilon_{n,s}^\eta(k_z) = \eta \sqrt{(\xi_n + s\chi_n)^2 + \Delta_n^2 \cos^2 \theta_n}, \quad n \geq 1, \quad (38)$$

$$\epsilon_0^\eta(k_z) = \eta(\gamma - \sqrt{b^2 + \Delta_0^2}), \quad n = 0, \quad (39)$$

where

$$\xi_n = \sqrt{2n\omega_B^2 + \gamma^2}; \quad \chi_n = \sqrt{b^2 + \Delta_n^2 \sin^2 \theta_n}; \quad (40)$$

$$\sin \theta_n = \frac{\gamma}{\xi_n}; \quad \cos \theta_n = \frac{\sqrt{2n\omega_B}}{\xi_n}; \quad (41)$$

$$\Delta_n(k_z) = \frac{t_S}{2} + \frac{t_D}{2} \cos(k_z d) - \omega_0 n. \quad (42)$$

The zero Landau levels in Eq. (39) clearly recover the Weyl nodes derived above.

VII. CONTINUUM LIMIT

Finally, we now consider the continuum limit of the TI thin film multilayer (Eq. 3). As mentioned above, one of the crucial differences between the present heterostructure and that of Burkov and Balents¹ is the $\hat{\Delta}(k_z, k_\perp)$ function, which is diagonal in the τ space. In the continuum limit we expand the $\hat{\Delta}(k_z, k_\perp)$ function near the Dirac point at $k_x = k_y = 0$, $k_z = \pi/d$ and obtain

$$\hat{\Delta}_c(k_z, k_\perp) = \left[\frac{t_S - t_D}{2} - t_\perp k_\perp^2 + \frac{\tilde{t}_D}{2} k_z^2 \right] \tau_z, \quad (43)$$

with $\tilde{t}_D = d^2 t_D / 2$ and we have rescaled $k_z \rightarrow k_z + \pi/d$. The continuum Hamiltonian can then be written as

$$\mathcal{H}_c(\mathbf{k}) = v_F(\hat{z} \times \boldsymbol{\sigma}) \cdot \mathbf{k}_\perp + \hat{\Delta}_c(k_z, k_\perp) \sigma_z. \quad (44)$$

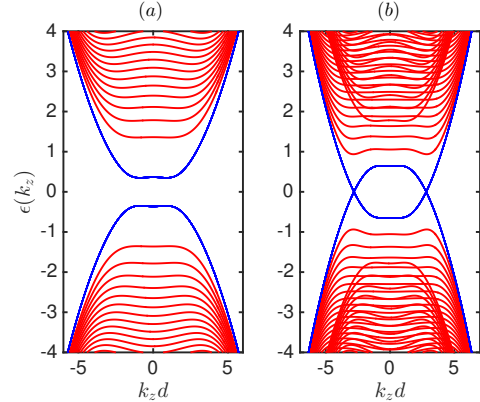


FIG. 5: Color online. The Landau level energy bands in the continuum limit (a) $\gamma = 0$; $b = 0.35$; (b) $\gamma = 1$, $b = 0.35$. All other parameters are $t_D = 0.5$, $t_S = 0.8t_D$, $t_\perp = 0.1$, $v_F = g = B = 1$. The universal constants e , c , μ_B are set to unity. The blue curves denote the zero Landau levels.

Using Eq. (44), it is readily seen that the Dirac nodes in the continuum limit are located at $\mathbf{k}^c = (0, 0, \pm k_z^c)$, where

$$k_z^c = \frac{1}{d} \sqrt{2(1 - t_S/t_D)}; \quad (45)$$

provided $t_S/t_D < 1$. Similar expression can be found for the general case $b, \gamma \neq 0$. Near the Dirac points, the dispersion is that of a massless 3D Dirac equation, given by

$$\epsilon_{\pm}(\mathbf{q}) \approx \pm \sqrt{v_F^2 q_x^2 + v_F^2 q_y^2 + \tilde{v}_F^2 q_z^2}, \quad (46)$$

where $\tilde{v}_F = \tilde{t}_D k_z^c$ and $\mathbf{q} = \mathbf{k} - \mathbf{k}^c$ is the momentum deviation from the Dirac nodes. Figure (5) shows the Landau levels in the continuum limit for $\gamma = 0$, $b \neq 0$ (a) and $\gamma \neq 0$, $b \neq 0$ (b). The Landau levels capture the appearance of Weyl (nodal) semimetal. We find no evidence of Weyl nodes for $\gamma = 0$, $b \neq 0$ as can be seen from the phase boundary in Eq. (26). Each pseudo spin sector ($\tau_z = \pm 1$) in Eq. (43) is the same as the continuum limit of the toy tight binding Hamiltonian of Weyl semimetal^{17–20}.

VIII. CONCLUSION

In this paper, we have studied a Weyl semimetal model first introduced by Burkov and Balents¹, but with an ultrathin film of topological insulator layers, whose Hamiltonian is different from that of the surface state of a

strong 3D topological insulator. In this new model, a 3D quantum spin Hall state emerged and the nodes of the Weyl semimetal occur at zero energy when time-reversal and inversion symmetries are broken. This new heterostructure can also be grown in the laboratory using ultrathin Bi_2Se_3 and Bi_2Te_3 films. Hence, it is experimentally accessible. Another important feature of the present model is that it reproduces previously studied toy tight binding models^{17–20} of Weyl semimetal in the continuum limit. Thus, it offers a physical realization of a Weyl semimetal phase in those systems. Thus, the ultra-thin film of topological insulator multilayer is another candidate for realizing Weyl semimetal phases (nodal semimetal) and quantum spin Hall state in three-dimensional electron systems.

Acknowledgement

We thank African Institute for Mathematical Sciences for hospitality. Research at Perimeter Institute is supported by the Government of Canada through Industry Canada and by the Province of Ontario through the Ministry of Research and Innovation.

* Electronic address: sowerre@perimeterinstitute.ca

- ¹ A. A. Burkov and L. Balents, Phys. Rev. Lett. **107**, 127205 (2011).
- ² A. A. Burkov, M. D. Hook, and L. Balents, Phys. Rev. B **84**, 235126 (2011).
- ³ G. B. Halász and L. Balents, Phys. Rev. B **85**, 035103 (2012).
- ⁴ S. Murakami, New J. Phys. **9**, 356 (2007).
- ⁵ X. Wan *et al.*, Phys. Rev. B **83**, 205101 (2011).
- ⁶ X. -L. Qi, T. L. Hughes, and S. -C. Zhang, Phys. Rev. B **78**, 195424 (2008); Phys. Rev. B **81**, 159901 (2010).
- ⁷ X. -L. Qi and S. -C. Zhang, Rev. Mod. Phys. **83**, 1057 (2011).
- ⁸ H. Zhang, *et al.*, Nature Phys. **5**, 438 (2009). L. Wu, *et al.* Nature Physics **9**, 410, 2013.
- ⁹ M. Z. Hasan and C. L. Kane, Rev. Mod. Phys. **82**, 3045 (2010); C. L. Kane and E. J. Mele, Phys. Rev. Lett. **95**, 226801 (2005).
- ¹⁰ B. A. Bernevig, T. L. Hughes, and S. -C. Zhang, Science **314**, 1757 (2006). M. Koenig, *et al.*, J. Phys. Soc. Jpn. **77**, 031007 (2008).
- ¹¹ F. R. Klinkhamer, G. E. Volovik, Int. J. Mod. Phys. **A20**, 2795 (2005); G. E. Volovik, The Universe in a Helium Droplet, Oxford University Press, (2003).
- ¹² A. A. Soluyanov, *et al.*, Nature **527**, 495 (2015).
- ¹³ W. Witczak-Krempa and Y. B. Kim, Phys. Rev. B **85**, 045124 (2012).
- ¹⁴ A. A. Zyuzin, M. D. Hook, A. A. Burkov, Phys. Rev. B **83**, 245428 (2011).
- ¹⁵ A. A. Zyuzin, S. Wu, and A. A. Burkov, Phys. Rev. B **85**, 165110 (2012).

- ¹⁶ C. -X. Liu, P. Ye, X. -L. Qi, Phys. Rev. B **87**, 235306 (2013); G. Y. Cho, arXiv:1110.1939 [cond-mat.str-el].
- ¹⁷ K.-Y. Yang, *et al.*, Phys. Rev. B **84**, 075129 (2011).
- ¹⁸ C. -Z. Chen, *et al.*, Phys. Rev. Lett. **115**, 246603 (2015).
- ¹⁹ H. -Z. Lu, S. -B. Zhang, and S. -Q. Shen, Phys. Rev. B **92**, 045203 (2015).
- ²⁰ P. Delplace, J. Li, D. Carpentier, EPL **97**, 67004 (2012).
- ²¹ L. Lu, *et al.*, Science, **349**, 622 (2015).
- ²² S. -Y. Xu, *et al.*, Science, **349**, 613 (2015).
- ²³ B. Q. Lv, *et al.*, Phys. Rev. X **5**, 031013 (2015).
- ²⁴ B. Q. Lv, *et al.*, Nature Physics **11**, 724 (2015).
- ²⁵ H. -Z. Lu, *et al.*, Phys. Rev. B **81**, 115407 (2010).
- ²⁶ H. Li, *et al.*, Phys. Rev. B **82**, 165104, (2010).
- ²⁷ H. Li, L. Sheng, and D. Y. Xing, Phys. Rev. B **85**, 045118 (2012); Phys. Rev. B **84**, 035310 (2012).
- ²⁸ W. -Y. Shan, H. -Z. Lu, and S. -Q. Shen, New J. Phys. **12**, 043048 (2010).
- ²⁹ Y. Sakamoto *et al.*, Phys. Rev. B **81**, 165432 (2010).
- ³⁰ Y. Zhang, *et al.*, Nature, **6**, 584 (2010).
- ³¹ J. Wang, *et al.*, Phys. Rev. B **83**, 245438 (2011).
- ³² S. -B. Zhang, H. -Z. Lu, S. -Q. Shen, Scientific Reports **5**, 13277 (2015).
- ³³ B. -J. Yang, T. Morimoto, and A. Furusaki, Phys. Rev. B **92**, 165120 (2015).
- ³⁴ Z. Wang, *et al.*, Phys. Rev. B **85**, 195320 (2012).
- ³⁵ Z. Wang, *et al.*, Phys. Rev. B **88**, 125427 (2013).
- ³⁶ S. M. Young, *et al.*, Phys. Rev. B **108**, 140405 (2012).
- ³⁷ L. Fu and C. L. Kane, Phys. Rev. B **76**, 045302 (2007).
- ³⁸ S. A. Owerre, and J. Nsofini, Solid State Commun. **218**, 35 (2015).